

Hadron Structure in Lattice QCD*

Constantia Alexandrou

Department of Physics, University of Cyprus, P.O. Box 20537, 1678 Nicosia,
Cyprus and
Computational-based Science and Technology Research Center, The Cyprus Institute,
P.O. Box 27456, 1645 Nicosia, Cyprus

August 27, 2018

Abstract

Recent progress in hadron structure calculations within lattice QCD is reviewed. Results on key observables such as the axial charge, the quark momentum fraction and the spin content of the nucleon are discussed with focus on open issues. Lattice QCD studies of the $\gamma^*N \rightarrow \Delta$ transition as well as the Δ form factors are also presented.

1 Introduction

The recent progress in the numerical simulation of the fundamental theory of the strong interactions, Quantum Chromodynamics (QCD), has been remarkable. Improvement in algorithms coupled with increase in computational power have enabled simulations to be carried out at near physical parameters of the theory. This opens up exciting possibilities for an *ab initio* calculation of experimentally measured quantities as well as for predicting quantities that are not easily accessible to experiment. During the last decade, results from simulations of QCD have emerged that already provide essential input for a wide range of strong interaction phenomena as, for example: i) The QCD phase diagram [1, 2, 3, 4] relevant for quark-gluon plasma searches at RHIC and LHC that probe the structure of our universe at $t \sim 10^{-32}$ s after the big-bang at temperatures $T \sim 10^{27}$ C; ii) The structure of hadrons [5, 6, 7, 8, 10, 11] that formed in our universe at $t \sim 10^{-6}$ s. Key hadronic properties such as the nucleon axial charge, the quark momentum distribution and spin content of the nucleon as well as form factors of other hadrons, resonances and decays are being investigated within the experimental programs of major facilities such as JLab, LHC and Mainz. iii) Nuclear forces [13] that determine the large scale structure of the universe $t \sim 10^9$ years after its birth. Although lattice QCD calculations of three- and four-baryon systems appeared recently, it is estimated that exa-scale computing resources will be required to extract accurate results and to extend to studies of light nuclei within lattice QCD [14].

In this work we will focus on hadron structure calculations [12] using state-of-the art lattice QCD simulations. After presenting some results that highlight the progress made in the meson sector, we will discuss the evaluation of key observables that probe the structure of the nucleon such as the form factors (FFs) and moments of generalized parton distributions (GPDs). Understanding nucleon structure from

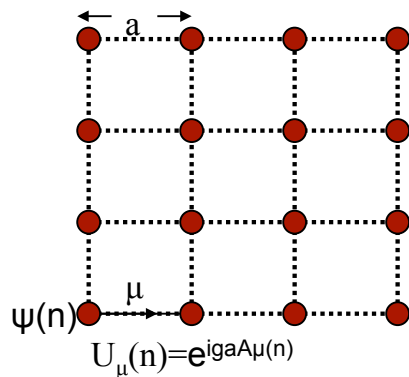
*Lecture presented at the Erice School on Nuclear Physics: *From Quarks and Gluons to Hadrons and Nuclei*, organized by A. Faessler and J. Wambach.

first principles is considered a milestones of hadronic physics and measurements of the electromagnetic nucleon form factors were first carried out more than 50 years ago. Despite their long history of measurements, recent double polarization experiments greatly improved the accuracy and revealed unexpected features, namely the ratio of the proton electric to magnetic form factor, $\mu_p G_E^p(q^2)/G_M^p(q^2)$, instead of being approximately constant, falls off almost linearly with the momentum transfer squared, q^2 [15]. This behavior is conjectured to be due to two-photon exchange terms that were previously neglected from the analysis [16] and it motivated new dedicated experiments to measure these form factors to higher precision and larger momentum transfers [17]. Compared to the electromagnetic (EM) form factors, the nucleon FFs connected to the axial-vector current are more difficult to measure and therefore less accurately known. An exception is the nucleon axial charge, g_A , which is precisely determined from neutron β -decay and provides a benchmark quantity for lattice QCD techniques.

Consequently we will present lattice QCD results on the $\gamma^*N \rightarrow \Delta$ transition. The $\gamma^*N \rightarrow \Delta$ is well studied experimentally as a probe of nucleon/ Δ deformation. In contrast to the nucleon and the $\gamma^*N \rightarrow \Delta$ FFs, the EM FFs of the Δ have not been measured, except from the Δ magnetic moment. Therefore they provide an ideal example of observables where lattice QCD can make predictions. We review these calculations as well as their implication on the shape of the Δ . Our study of the Δ and N to Δ systems include the corresponding matrix elements of the axial-vector current that provide information on the axial couplings used in chiral expansions.

2 Introduction to Lattice QCD

Before we explain how the relevant hadronic matrix elements are determined we briefly outline the lattice formalism that enables their extraction.



The starting point is a definition of the theory on a four-dimensional Euclidean space-time lattice. The lattice acts as a non-perturbative regularization scheme with the lattice spacing a providing an ultraviolet cutoff at highest allowed momentum π/a . Gauge fields are defined as links $U_\mu(n)$ between adjacent lattice sites and quarks are defined at each lattice site as anticommuting Grassmann variables belonging to the fundamental representation of $SU(3)$.

Using these fundamental quark and gluons degrees of freedom one constructs an appropriate action such that when $a \rightarrow 0$ (and the lattice volume $\rightarrow \infty$) one recovers the continuum theory. The construction of the appropriate operators with their renormalization is then carried out in order to extract physical quantities. This discrete formulation of QCD in Euclidean time is referred to as lattice QCD (LQCD). It can be simulated on the computer using methods analogous to those used in Statistical Mechanics allowing calculation of matrix elements of any operator between hadronic states in terms of the fundamental quark and gluon degrees of freedom. LQCD, therefore, provides a well-defined approach to calculate observables non-perturbatively starting directly from the QCD Lagrangian with only input parameters the coupling constant and the quark masses.

In what follows we will show results obtained on an isotropic hypercubic grid taking the spatial distance between lattice sites a_S to be the same as the temporal one a_T i.e. $a = a_S = a_T$. We will also limit ourselves to zero temperature taking the spatial size L_S less than the temporal size L_T . Anisotropic lattices where $a_S > a_T$ are also being used mainly for the study of excited states [18, 19]. Although LQCD provides an *ab initio* calculation of hadronic properties, the discretization of space-time and the numerical simulation on a finite volume introduce artifacts that may lead to systematic errors, which

must be carefully investigated before comparing to experimental results. Of particular relevance, for the observables discussed in this work, are the following issues: i) *Finite Volume*: One needs to perform simulations on different volumes to study finite volume effects. Volume studies of observables considered here, have shown that finite effects are small for lattice sizes such that $L_S m_\pi \gtrsim 3.5$. A consequence of having a finite volume is that only discrete values of momentum are allowed. For periodic boundary conditions (b.c.) the momenta allowed are in units of $2\pi/L_S$. Twisted b.c. have been used to obtain observables at small non-zero momenta. ii) *Finite lattice spacing*: LQCD simulations for at least three values of the lattice spacing are needed in order to extrapolate results to the continuum limit. iii) *Renormalization constants*: Computation of the appropriate renormalization constants is needed in order to relate lattice matrix elements to continuum results. iv) *Heavier than physical pion masses*: Current LQCD results are obtained using simulations that are typically performed at heavier than physical pion masses requiring chiral extrapolation. However, simulations with pions at their physical mass have been achieved [20] and more are foreseen in the near future. v) *Fourier transforms*: One needs to Fourier transform lattice results computed in coordinate space numerically. For large values of momentum transfer, results become noisy and typically only values of momentum transfer squared $Q^2 = -q^2 \sim 2 \text{ GeV}^2$ can be achieved.

2.1 Lattice techniques

In this section we briefly explain how hadron masses and matrix elements of local operators are computed. Like the continuum theory, the QCD lattice action can be written as $S = S_g + S_F$, where S_g contains a purely gluonic part, written in terms of the gauge links U_μ , and S_F contains the kinetic energy of the quarks and the interaction terms. The fermionic action is bi-linear in the quark fields $\psi(x)$ i.e. $S_F = \sum_{n,j} \bar{\psi}(n) D_{nj} \psi(j)$, where n and j denote the lattice sites. The exact form of the lattice Dirac matrix, D , depends on the discretization scheme used for the fermions. Within the Feynman path integral representation the vacuum expectation value of a gauge invariant operator \mathcal{B} is given by

$$\langle \Omega | \mathcal{B} | \Omega \rangle = \frac{\int d[U] d[\bar{\psi}] d[\psi] B[U, \bar{\psi}, \psi] e^{-S_g[U] - S_F[U, \bar{\psi}, \psi]}}{\int d[U] d[\bar{\psi}] d[\psi] e^{-S_g[U] - S_F[U, \bar{\psi}, \psi]}}. \quad (1)$$

After integrating over the fermionic degrees of freedom, one obtains

$$\langle \Omega | \mathcal{B} | \Omega \rangle = \frac{1}{Z} \int d[U] \det(D[U]) \mathbf{B}[U, D^{-1}[U]] e^{-S_g[U]}, \quad Z \equiv \int d[U] \det(D[U]) e^{-S_g[U]}, \quad (2)$$

in which the fermionic determinant appears and we obtain a factor of $D_{jn}^{-1}[U]$ for each possible Wick contraction of fermion pairs $-\bar{\psi}_n \psi_j$. One performs the path integrals numerically by stochastically generating a representative ensemble of N gauge configurations $\{U\}$ according to the probability $\exp\{-S_g[U] + \ln(\det(D[U]))\}/Z$ given in Eq. (2) and then averaging over these gauge configurations:

$$\langle \Omega | \mathcal{B} | \Omega \rangle = \lim_{N \rightarrow \infty} \frac{1}{N} \sum_{k=1}^N B[U^k, D^{-1}[U^k]] \quad . \quad (3)$$

The time consuming part of a LQCD calculation related to hadron properties is the generation of an ensemble of gauge configurations and the computation of the inverse of the fermionic matrix D , which yields the quark propagator¹. In many applications only a column of D^{-1} is required. However, in calculating e.g. the isoscalar nucleon FFs the full (spatial) inverse is needed as these involve diagrams where an external probe couples to a sea quark. Calculation of these fermionic loops is therefore much more difficult and results on the observables presented in this work have not taken into account these contributions. Historically, LQCD simulations were done in the quenched approximation that sets $\det(D) = 1$ in Eq. (2) leaving a local action $S_g[U]$ making such simulations much easier. Nowadays, however, unquenched simulations are performed, which include the $\det(D)$.

¹In multi-baryon systems the contractions needed for the computation of observables is also a time-consuming step [14].

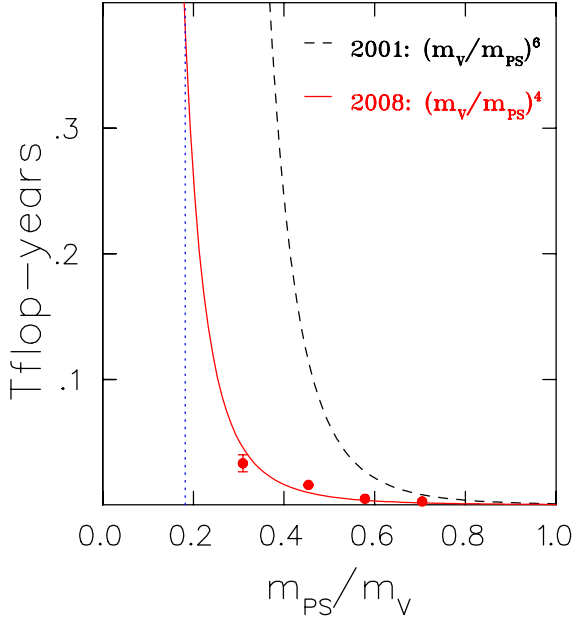


Figure 1: Simulation cost of TMF using $L_S = 2.1$ fm, $a = 0.089$ fm as a function of the pion mass to the ρ -meson mass [21]. The physical point is showed by the dotted horizontal line.

2.2 Recent results

2.2.1 Spectrum of low-lying baryons

Masses of low-lying hadrons are extracted from the vacuum expectation value of two-point functions:

$$G(t, \vec{p}) = \sum_{\vec{x}} e^{-i\vec{p}\cdot\vec{x}} \langle \Omega | \Gamma_{\beta\alpha}^4 T \chi_h^\alpha(\vec{x}, t) \bar{\chi}_h^\beta(\vec{0}, 0) | \Omega \rangle, \quad (4)$$

with the projection matrix $\Gamma^4 = (1 + \gamma^4)/2$. The interpolating fields, $\chi_h(x)$, are operators in the Heisenberg representation that create a trial state with the quantum numbers of the hadron h that we want to study. The spectral decomposition of the two-point function, in the infinite lattice size limit,

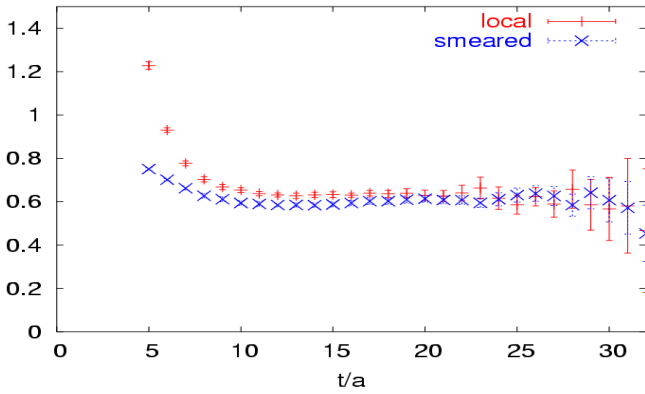


Figure 2: Nucleon effective mass using local and smeared interpolating fields.

The cost of these simulations can be estimate by using the cost formula:

$$C_{\text{sim}} \propto \left(\frac{300 \text{ MeV}}{m_\pi} \right)^{c_m} \left(\frac{L}{2 \text{ fm}} \right)^{c_L} \left(\frac{0.1 \text{ fm}}{a} \right)^{c_a},$$

where the coefficients c_m , c_L and c_a depend on the type of discretization used for the fermionic action. State-of-the-art simulations use improved algorithms that take advantage of the mass preconditioner trick [22] and use multiple time scales in the molecular dynamics updates. These improvements reduce the required simulation time making simulations at the physical value of the pion mass (physical point) feasible. The cost for generating 10^3 independent $N_f = 2$ twisted mass fermions (TMF) gauge configurations as the pion mass decreases at fixed a and L_S is shown in Fig. 1. One finds $c_m \sim 4$ in contrast to $c_m \sim 6$ that characterized Wilson fermion simulations ten years ago. Based on current simulations the cost at the physical point is estimated to be $\mathcal{O}(1)$ Teraflop-year.

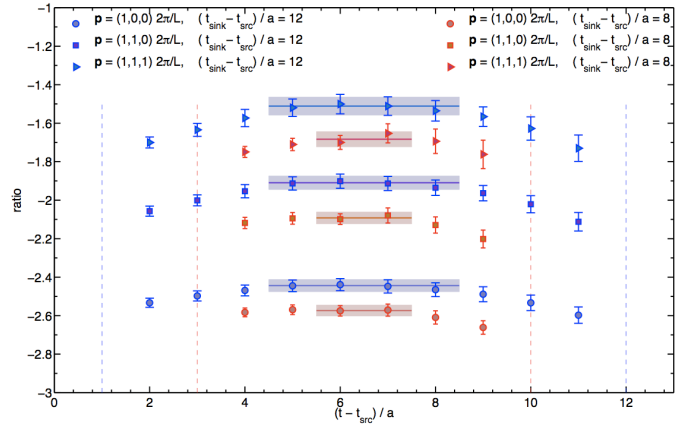


Figure 3: Ratio of nucleon three-point to two-point functions for two sink-source separations as a function of the current insertion time $(t - t_i)/a$.

can be written as

$$G(t, \vec{p}) = \sum_n |\langle \Omega | \chi_h | n(\vec{p}) \rangle|^2 e^{-E_n(\vec{p})t} \quad t \gg \frac{1}{\vec{p}=0} \mathcal{Z}_h(\vec{0}) e^{-m_0 t} \quad , \quad (5)$$

where $E_n(\vec{p})$ is the energy of the n^{th} state. For single particle states $E_n(\vec{p}) = \sqrt{m_n^2 + \vec{p}^2}$. By $|h\rangle$ we denote the lowest eigenstate of QCD with the quantum numbers of χ_h with mass m_0 obtained by setting $\vec{p} = \vec{0}$ in Eq. (5) and overlap $\mathcal{Z}_h(\vec{0}) = |\langle \Omega | \chi_h | h(\vec{0}) \rangle|^2$ with the trial state $\chi_h^\dagger | \Omega \rangle$. For large time separation t between the source and the sink the unknown overlap factor $|\langle \Omega | \chi_h | h(\vec{0}) \rangle|^2$ and exponential time dependence cancel in the ratio $m_{\text{eff}}(t) = -\log [G(t, \vec{0})/G(t-1, \vec{0})]$, which therefore becomes time independent (plateau region) and can be fitted to a constant to yield m_0 . This is demonstrated in Fig. 2, where we show the nucleon effective mass as a function of t/a obtained using local interpolating fields and smeared ones. Smearing creates a quark field with support at several lattice sites instead of at one. It is a technique used to optimize the overlap \mathcal{Z}_h with the ground state achieving faster ground state dominance as shown in Fig. 2. For the numerical evaluation of such two-point functions one needs quark propagators from the fixed source $(\vec{0}, 0)$ to all spatial \vec{x} -sink points for several time separations. This requires the computation of only one column for each spin/color component of the quark propagator, namely $v(\vec{x}, t) \equiv D^{-1}(\vec{x}, t; \vec{0}, 0)$ obtained by solving the equation $D(y, x)v(x) = \delta(y - (\vec{0}, 0))$.

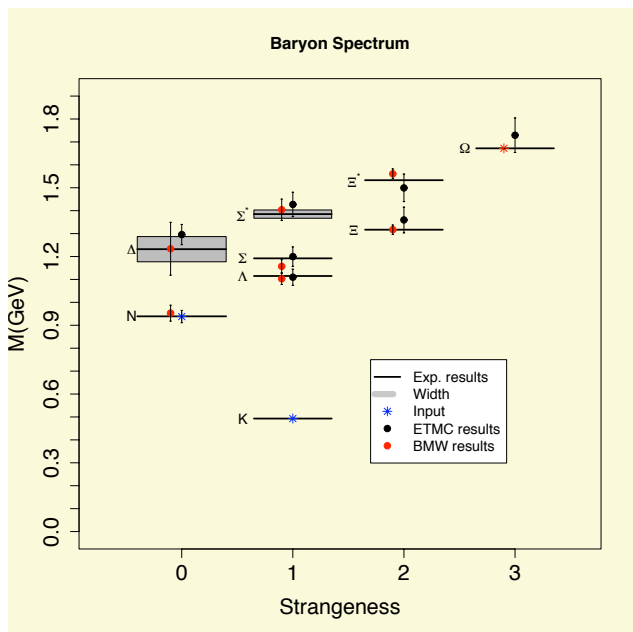


Figure 4: The low-lying baryon spectrum computed using $N_f = 2 + 1$ Clover [23] and $N_f = 2$ TMF [24].

2.2.2 Hadron form factors

Calculation of hadron matrix elements is more involved and requires the evaluation of a three-point function, depicted schematically in Figs. 5 and 6. The corresponding expression for the nucleon three-point function is

$$G_{\mu\nu}(\Gamma, \vec{q}, t) = \sum_{\vec{x}_f, \vec{x}} e^{i\vec{x}\cdot\vec{q}} \langle \Omega | \Gamma_{\beta\alpha} \chi_n^\alpha(\vec{x}_f, t_f) \mathcal{O}_{\mu\nu}(\vec{x}, t) \bar{\chi}_n^\beta(0) | \Omega \rangle \quad . \quad (6)$$

We first comment on the evaluation of the connected diagram. From Eq. (6) it is clear that two spatial sums are involved, one over the spatial coordinates of the operator and one over the spatial coordinates of

In Fig. 4 we show recent results on the low-lying baryon spectrum obtained using two types of Wilson improved fermion action S_F . The BMW Collaboration uses a Clover term in S_F and smeared gauge links. Simulations were performed with two degenerate u- and d-quarks and a strange quark fixed to its physical mass ($N_f = 2 + 1$) using the mass of the Ω . The ETM Collaboration uses a twisted mass term in S_F , which provides automatic $\mathcal{O}(a)$ improvement, and $N_f = 2$. The strange valence quark mass was fixed using the kaon mass. Both collaborations analyzed configurations generated at 3 lattice spacings: $a = 0.125, 0.085, 0.065$ fm determined by the Ξ -mass in the case of BMW and $a = 0.089, 0.070, 0.056$ fm, set by the nucleon mass in the case of ETMC and extrapolated the results to the continuum limit and to the physical pion mass. One observes that the results using different discretization schemes are in agreement and that both reproduce the experimental values. This is a significant validation of LQCD techniques.

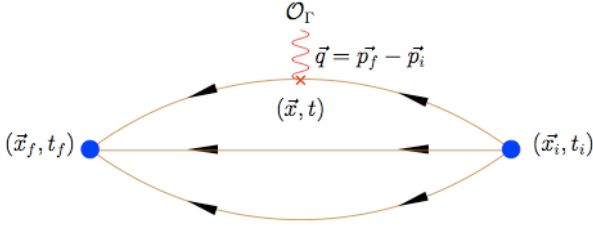


Figure 5: Connected three-point function.

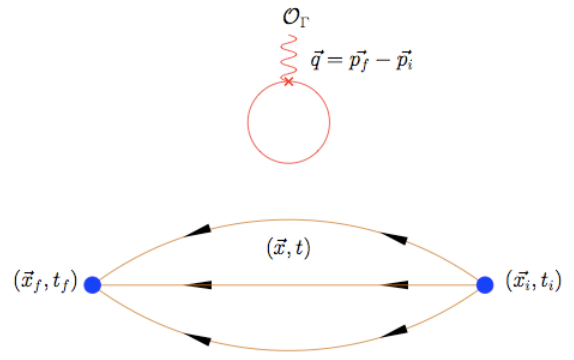


Figure 6: Disconnected three-point function.

the final state. This means that the propagator from the operator insertion, denoted by \vec{x} in Figs. 5 and 6, to the sink, denoted by \vec{x}_f , involves all spatial columns of D^{-1} . The trick to evaluate this inverse is to perform the sum over \vec{x}_f by solving the equation $D(x_f, x)\mathcal{V}(x) = S(x_f) \rightarrow \mathcal{V}(x) = \sum_{x_f} D^{-1}(x, x_f)S(x_f)$ with an appropriately constructed source $S(x_f)$ that combines the two quark propagators from the fixed source at t_i with the hadron state at t_f . The solution $\mathcal{V}(x)$ is the sequential (backward) propagator from the sink to the operator with the summation over \vec{x}_f done automatically. Using the symmetries of the Dirac operator the forward sequential propagator can be easily constructed. This so called ‘fixed sink method’ is used in most recent calculations of three-point functions and takes its name from the fact that the quantum numbers of the hadron state at the sink enter into the construction of the sequential propagator and must therefore be fixed. It also requires fixing the sink-source time separation $t_f - t_i$, final momentum \vec{p}_f and spin projection matrix Γ . Inserting the operator, which can be done at all values of \vec{x} , and summing over with the appropriate Fourier phase and propagator starting at t_i and ending at t yields the connected three-point function. Therefore, within this scheme and for each non-degenerate quark flavor, two inversions involving the Dirac matrix enable one to compute the three-point function for all possible momentum transfers \vec{q} and operators \mathcal{O} .

To extract the nucleon matrix element $\langle N(\vec{p}_f) | \mathcal{O} | N(\vec{p}_i) \rangle$ we study the large Euclidean time behavior of an appropriately defined ratio of the three-point function and two-point functions [12] given by

$$R^{\mu\nu}(\Gamma, \vec{q}, t) = \frac{G^{\mu\nu}(\Gamma, \vec{q}, t)}{G(\vec{0}, t_f)} \sqrt{\frac{G(\vec{p}_i, t_f - t)G(\vec{0}, t)G(\vec{0}, t_f)}{G(\vec{0}, t_f - t)G(\vec{p}_i, t)G(\vec{p}_i, t_f)}} \xrightarrow{t \gg 1} \Pi^{\mu\nu}(\vec{q}, \Gamma) \quad , \quad (7)$$

where we have set $\vec{p}_f = \vec{0}$. Like in the case of the effective mass, this ratio is defined so that the unknown overlaps $\mathcal{Z}_n(\vec{p})$ as well as the time dependence arising from the time evolution cancel, yielding a time independent quantity (plateau), which signals identification of the nucleon state from the tower of QCD states with the same quantum numbers as the nucleon. Fitting to this plateau value we can extract the matrix element $\langle N(p_f) | \mathcal{O} | N(p_i) \rangle$ and from this, depending on the choice of \mathcal{O} , the FFs or moments of GPDs. However, the identification of the plateau region is much more delicate as compared to the case of the effective mass. This is demonstrated in Fig. 3 where we show results for two sink-source time separations. As can be seen, while one might think that there is already a plateau for the smaller time separation, increasing the sink-source separation changes the value of the plateau, which in turn means that excited states still contribute significantly. For the nucleon form factors and pion masses larger than about 300 MeV one has found that $t_f - t_i \gtrsim 1$ fm is sufficient.

Several collaborations, using dynamical quarks with pion mass down to about 300 MeV, have calculated the pion electromagnetic (EM) form factor [25], which is obtained from the matrix element $\langle \pi^+(p_f) | J_\mu | \pi^+(p_i) \rangle = (p_{f\mu} + p_{i\mu})F_\pi(q^2)$, where $q^2 = (p_f - p_i)^2 = -Q^2$. Recent results are shown in Fig. 7 [26]. Based on vector dominance, lattice data are fitted to the form $F_\pi(Q^2) = (1 + \langle r^2 \rangle Q^2/6)^{-1}$ to extract the mean squared radius, which is shown in Fig. 8. As can be seen, there is an increase in the value of $\langle r^2 \rangle$ at small pion mass, m_π . An accurate extraction of $\langle r^2 \rangle$ benefits from evaluating the

form factor at small values of Q^2 accomplished by using twisted b.c. In a recent calculation, ETMC combined twisted b.c. and the so called ‘one-end’ trick to incorporate the all-to-all propagator and improve statistics. Using $N_f = 2$ simulations with twisted mass fermions at two lattice spacings and two volumes [27] the assessment of cut-off and volume effects was carried out. LQCD results on F_π estimated in the continuum limit at pion masses in the range of 300 MeV to 500 MeV, are extrapolated to the physical point using NNLO chiral perturbation theory (PT). The resulting form factor is shown in Fig. 9 [27] and it is in agreement with experiment.

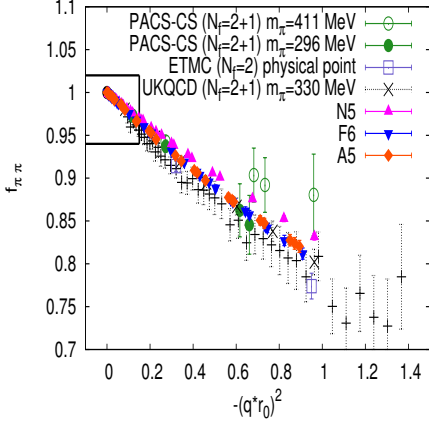


Figure 7: Recent LQCD results on F_π as a function of q^2 [26] in units of the scale r_0 [28].

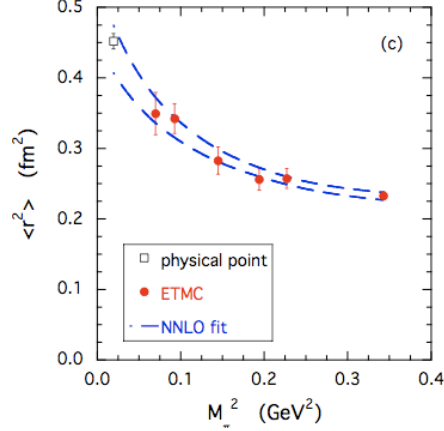


Figure 8: The pion mean square radius as a function of m_π^2 with $N_f = 2$ TMF.

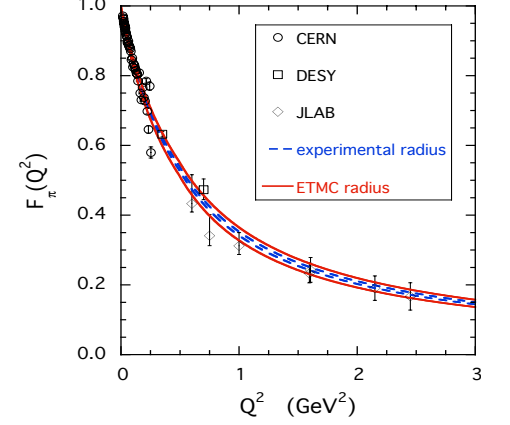


Figure 9: F_π at the physical pion mass (red band) compared to experiment (blue).

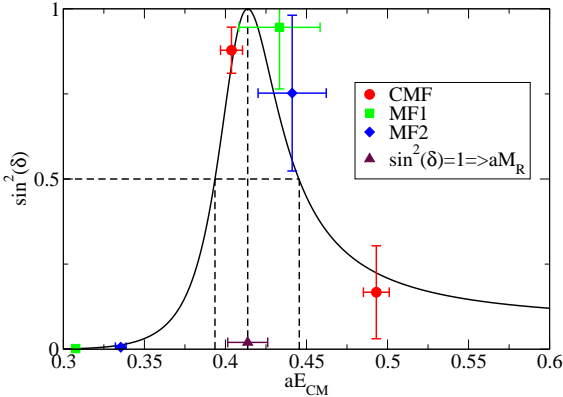


Figure 10: The ρ -meson phase shift at $m_\pi = 308$ MeV for a lattice of $L_S = 2.8$ fm.

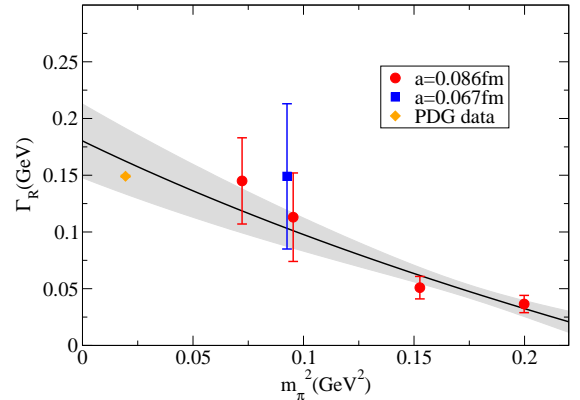


Figure 11: The ρ -meson width for $N_f = 2$ twisted mass fermions as a function of m_π^2 .

As simulations with quark masses close to the physical value become available, the study of resonances and decays of unstable particles becomes an important issue. The ρ -meson width has been studied by several groups [29]. Considering a $\pi^+\pi^-$ system in the $I = 1$ -channel, the P-wave scattering phase shift $\delta_{11}(k)$ in infinite volume is related via Lüscher’s relation to the energy shift in a finite box. Using $N_f = 2$ TMF and considering the center of mass frame and two moving frames one extracts the phase shift at different values of the energy, shown in Fig. 10. From the effective range formula $\tan \delta_{11}(k) = \frac{g_{\rho\pi\pi}^2}{6\pi} \frac{k^3}{E_{CM}(m_R^2 - E_{CM}^2)}$, where $k = \sqrt{E_{CM}^2/4 - m_\pi^2}$ one determines m_R and the coupling $g_{\rho\pi\pi}$ and then extracts the width using $\Gamma_\rho = \frac{g_{\rho\pi\pi}^2}{6\pi} \frac{k_R^3}{m_R^2}$, where $k_R = \sqrt{m_R^2/4 - m_\pi^2}$. The results on the width as a function of m_π^2 are shown in Fig. 11 [30].

2.3 Disconnected contributions

Recently, progress has been made in the evaluation of the disconnected contributions to the three-point functions using stochastic techniques [31, 32]. A case study was carried out to compare various stochastic methods to the exact evaluation enabled using graphics cards. For this test case, $N_f = 2$ Wilson fermions simulated by the SESAM Collaboration on a volume of $16^3 \times 32$ at $m_\pi \sim 750$ MeV were used. In Figs. 12 and 13 we show results on the connected and disconnected contributions to the nucleon magnetic and scalar FFs, respectively. As can be seen, the disconnected contribution to the the magnetic FF is consistent with zero, whereas to the scalar FF is of the same order as the connected one. Furthermore, the scalar disconnected part converges with much fewer stochastic noise vectors as compared to disconnected loops contributing to the nucleon FFs, which show slow convergence [33]. A particularly suitable method for evaluating these fermionic loops is the truncated solver method [31].

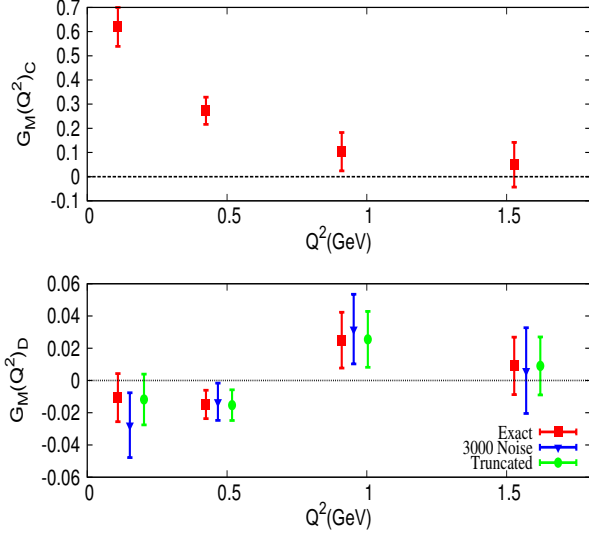


Figure 12: Connected (upper) and disconnected (lower) contributions to the nucleon magnetic FF.

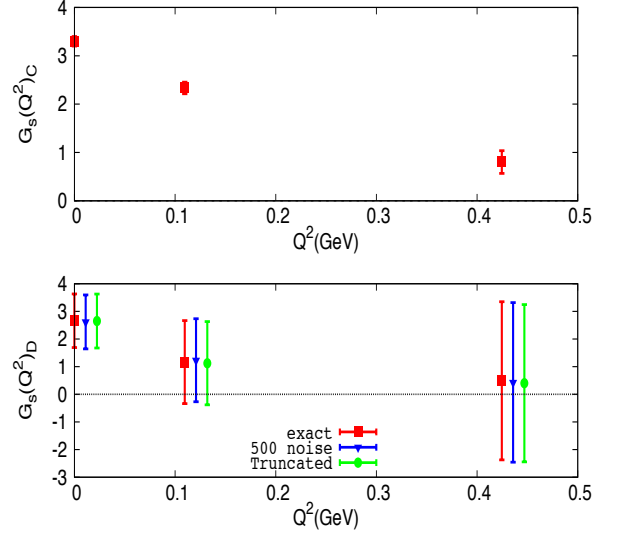


Figure 13: Connected (upper) and disconnected (lower) contributions to the nucleon scalar FF.

3 Nucleon Generalized form factors

High energy scattering can be formulated in terms of light-cone correlation functions. Considering one-particle states $|p'\rangle$ and $|p\rangle$, GPDs are defined by [8, 9]:

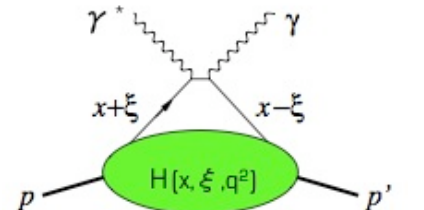
$$F_\Gamma(x, \xi, q^2) = \frac{1}{2} \int \frac{d\lambda}{2\pi} e^{ix\lambda} \langle p' | \bar{\psi}(-\lambda n/2) \Gamma \mathcal{P} e^{ig \int_{-\lambda/2}^{\lambda/2} d\alpha n \cdot A(n\alpha)} \psi(\lambda n/2) | p \rangle, \quad (8)$$

where $\bar{P} = (p' + p)/2$, $\xi = -n \cdot q/2$, x is the momentum fraction, and n is a light-cone vector with $\bar{P} \cdot n = 1$.

There are three different types of operators, depending on the choice of Γ . Considering nucleon states these are:

$$\begin{aligned} \Gamma &= \not{n} \rightarrow \frac{1}{2} \bar{u}_N(p') \left[\not{n} H(x, \xi, q^2) + i \frac{n_\mu q_\nu \sigma^{\mu\nu}}{2m_N} E(x, \xi, q^2) \right] u_N(p) \\ \Gamma &= \not{n} \gamma_5 \rightarrow \frac{1}{2} \bar{u}_N(p') \left[\not{n} \gamma_5 \tilde{H}(x, \xi, q^2) + \frac{n \cdot q \gamma_5}{2m_N} \tilde{E}(x, \xi, q^2) \right] u_N(p) \\ \Gamma &= n_\mu \sigma^{\mu\nu} \rightarrow \text{tensor GPDs} \end{aligned}$$

“Handbag” diagram



The forward proton matrix elements $F_\Gamma(x, 0, 0)$, measured in deep inelastic scattering, are connected

to the parton distributions $q(x)$, $\Delta q(x)$, $\delta q(x)$. Expansion of the light cone operator leads to a tower of local twist-2 operators $\mathcal{O}_F^{\mu\mu_1\dots\mu_n}$, the forward matrix elements of which are related to moments:

$$\begin{aligned}\mathcal{O}_q^{\mu\mu_1\dots\mu_n} &= \bar{\psi}\gamma^{\{\mu}iD^{\mu_1}\dots iD^{\mu_n\}\psi} \xrightarrow{\text{unpolarized}} \langle x^n \rangle_q = \int_0^1 dx x^n [q(x) - (-1)^n \bar{q}(x)] \\ \tilde{\mathcal{O}}_{\Delta q}^{\mu\mu_1\dots\mu_n} &= \bar{\psi}\gamma_5\gamma^{\{\mu}iD^{\mu_1}\dots iD^{\mu_n\}\psi} \xrightarrow{\text{helicity}} \langle x^n \rangle_{\Delta q} = \int_0^1 dx x^n [\Delta q(x) + (-1)^n \Delta \bar{q}(x)] \\ \mathcal{O}_{\delta q}^{\rho\mu\mu_1\dots\mu_n} &= \bar{\psi}\sigma^{\rho\{\mu}iD^{\mu_1}\dots iD^{\mu_n\}\psi} \xrightarrow{\text{transversity}} \langle x^n \rangle_{\delta q} = \int_0^1 dx x^n [\delta q(x) - (-1)^n \delta \bar{q}(x)]\end{aligned}$$

where $q = q_\downarrow + q_\uparrow$, $\Delta q = q_\downarrow - q_\uparrow$, $\delta q = q_\top + q_\perp$, and the curly brackets represent a symmetrization over indices and subtraction of traces. The off-diagonal matrix elements extracted from deep virtual Compton scattering can be written in terms of generalized form factors (GFFs), which contain both form factors and parton distributions:

$$\begin{aligned}\langle N(p', s') | \mathcal{O}_q^{\mu\mu_1\dots\mu_n} | N(p, s) \rangle &= \bar{u}_N(p', s') \left[\sum_{i=0,2,\dots}^n \left(A_{n+1,i}(q^2) \gamma^{\{\mu} + B_{n+1,i}(q^2) \frac{i\sigma^{\{\mu\alpha} q_\alpha}{2m} \right) } q^{\mu_1} \dots q^{\mu_i} \bar{P}^{\mu_{i+1}} \dots \bar{P}^{\mu_n} \right. \\ &\quad \left. + \text{mod}(n, 2) C_{n+1,0}(q^2) \frac{1}{m} q^{\{\mu} q^{\mu_1} \dots q^{\mu_n\}} \right] u_N(p, s)\end{aligned}\quad (9)$$

and similarly for $\mathcal{O}_{\Delta q}^{\mu\mu_1\dots\mu_n}$ (in terms of $\tilde{A}_{ni}(q^2)$, $\tilde{B}_{ni}(q^2)$) and $\mathcal{O}_{\delta q}^{\rho\mu\mu_1\dots\mu_n}$ (in terms of A_{ni}^T , B_{ni}^T , C_{ni}^T , D_{ni}^T). In this work we will show results on the following special cases:

- $n = 1$: Ordinary nucleon form factors:

$$\begin{aligned}A_{10}(q^2) = F_1(q^2) &= \int_{-1}^1 dx H(x, \xi, q^2), & B_{10}(q^2) = F_2(q^2) &= \int_{-1}^1 dx E(x, \xi, q^2) \\ \tilde{A}_{10}(q^2) = G_A(q^2) &= \int_{-1}^1 dx \tilde{H}(x, \xi, q^2), & \tilde{B}_{10}(q^2) = G_p(q^2) &= \int_{-1}^1 dx \tilde{E}(x, \xi, q^2),\end{aligned}$$

where in the case of the EM current, $j_\mu = \bar{\psi}(x)\gamma_\mu\psi(x)$, the nucleon matrix element is written in the form $\bar{u}_N(p', s') [\gamma_\mu F_1(q^2) + \frac{i\sigma_{\mu\nu} q^\nu}{2m_N} F_2(q^2)] u_N(p, s)$. The Dirac F_1 and Pauli F_2 FFs are related to the electric and magnetic Sachs FFs via the relations: $G_E(q^2) = F_1(q^2) - \frac{q^2}{(2m_N)^2} F_2(q^2)$ and $G_M(q^2) = F_1(q^2) + F_2(q^2)$. For the axial-vector current $A_\mu^a = \bar{\psi}(x)\gamma_\mu\gamma_5\frac{\tau^a}{2}\psi(x)$ the nucleon matrix element is of the form $\bar{u}_N(p', s') [\gamma_\mu\gamma_5 G_A(q^2) + \frac{q_\mu\gamma_5}{2m_N} G_p(q^2)] \frac{1}{2} u_N(p, s)$, where $G_A(0) = g_A$ is the nucleon axial charge.

- $A_{n0}(0)$, $\tilde{A}_{n0}(0)$, $A_{n0}^T(0)$ are moments of parton distributions, e.g. $\langle x \rangle_q = A_{20}(0)$ and $\langle x \rangle_{\Delta q} = \tilde{A}_{20}(0)$ are the first moments of the unpolarized and helicity distributions. Knowing these quantities one can evaluate the quark spin, $J_q = \frac{1}{2}[A_{20}(0) + B_{20}(0)] = \frac{1}{2}\Delta\Sigma_q + L_q$ and investigate the fraction of the spin carried by quarks and its contribution to the total spin via the nucleon spin sum rule, $\frac{1}{2} = \frac{1}{2}\Delta\Sigma_q + L_q + J_g$, as well as the momentum fraction carried by gluons via the momentum sum rule: $\langle x \rangle_g = 1 - A_{20}(0)$.

In order to compare LQCD matrix elements to physical observables we need to renormalize them. Most collaborations carry out a non-perturbative evaluation of the vertex function $\Gamma_{\mu\nu}(p)$. The renormalization constants can be determined in the RI'-MOM scheme by imposing the following conditions

$$Z_q = \frac{1}{12} \text{Tr}[(G(p))^{-1} G^{(0)}(p)] \Big|_{p^2=\mu^2}, \quad Z_q^{-1} Z_{\mathcal{O}} \frac{1}{12} \text{Tr}[\Gamma_{\mu\nu}(p) \Gamma_{\mu\nu}^{(0)-1}(p)] \Big|_{p^2=\mu^2} = 1, \quad (10)$$

to extract Z_q and $Z_{\mathcal{O}}$. Subtracting $\mathcal{O}(a^2)$ -terms perturbatively improves their determination at the continuum limit [34].

3.1 Results on nucleon form factors

A number of lattice QCD groups have recently produced results on nucleon FFs employing dynamical quark simulations with $\mathcal{O}(a)$ -improved actions and lowest pion mass typically round ~ 300 MeV [12].

• **Nucleon axial charge:** The axial charge is well known experimentally. Since it can be determined at $Q^2 = 0$ there is no ambiguity associated with having to fit the Q^2 -dependence of a FF, such as, for example, in the case of the anomalous magnetic moment where one needs to fit the small Q^2 -dependence of the magnetic FF G_M . In addition, only the connected diagram shown in Fig. 5 contributes. In Fig. 14 we show recent LQCD results using TMF, Clover fermions, domain wall fermions (DWF) and a hybrid action of DWF on a staggered sea, all of which are renormalized non-perturbatively. As can be seen, there is a nice agreement among different lattice discretizations and no significant dependence on the quark mass down to about $m_\pi = 270$ MeV.

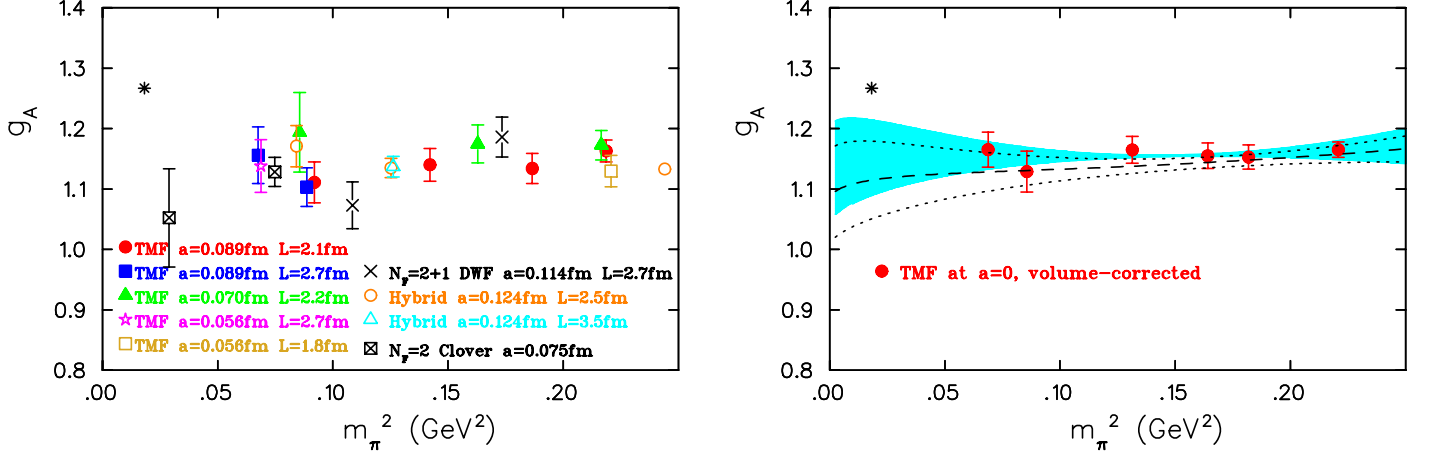


Figure 14: Left: LQCD results on g_A using $N_f = 2$ TMF [35] (filled symbols, star and open square), $N_f = 2 + 1$ DWF [36] (crosses), $N_f = 2 + 1$ hybrid action [37] (open circles and triangle) and $N_f = 2$ Clover [38] (square with cross). The experimental value is shown by the asterisk. Right: Volume corrected TMF results extrapolated to the continuum limit together with a chiral fit using HB χ PT (blue band). The band bounded by the lines is the chiral fit to the TMF data shown on the left panel.

To assess lattice artifacts and obtain a value of g_A at the physical point, we use LQCD results obtained with TMF [35]. The volume corrected [39] data are extrapolated to $a = 0$ using three lattice spacings, namely $a = 0.089$ fm, 0.070 fm and 0.056 fm. The continuum volume-corrected results are shown in Fig. 14. A chiral extrapolation using one-loop heavy baryon chiral perturbation theory (HB χ PT) in the small scale expansion (SSE) [40] with three fit parameters produces a value of $g_A = 1.12(8)$ at the physical point, which is lower than the experimental value by about a standard deviation. The large error is due to the strong correlation between the Δ axial charge and the counter-term involved in the fit. In Sec. 5 we discuss the evaluation of the Δ axial charge within LQCD and examine the resulting chiral extrapolation. Fitting the uncorrected LQCD results obtained at the three β -values produces the band shown by the dotted lines. This indicates that, for pion masses larger than ~ 300 MeV, volume and discretization errors are small compared to the uncertainty in the chiral extrapolation.

• **Nucleon form factors:** Recent LQCD results on the EM isovector and axial FFs are shown in Fig. 15. We observe a nice agreement among LQCD results, in particular for $G_E(Q^2)$ and $G_A(Q^2)$. However, both $G_E(Q^2)$ and $G_A(Q^2)$ decrease with increasing Q^2 less rapidly than measured in experiment. We note that a good description of the Q^2 -dependence for both $G_E(Q^2)$ and $G_M(Q^2)$ is provided by a dipole form using the lattice-computed ρ -meson mass. If one uses HB χ PT to one-loop, with explicit Δ degrees to perform a chiral extrapolation of the Pauli and Dirac form factors at small Q^2 -values then one qualitatively recovers the correct slope of the experimental data [41]. LQCD on $G_p(Q^2)$ using

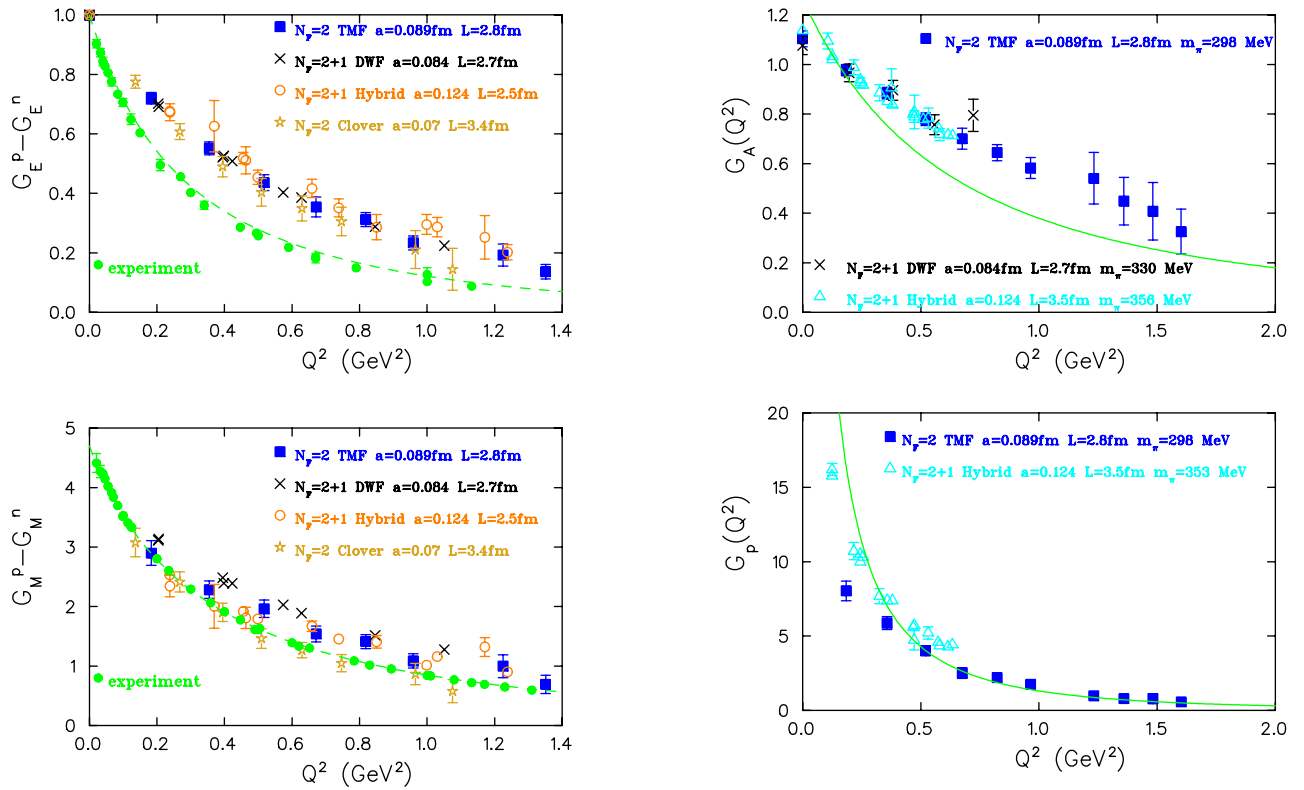


Figure 15: Left: Isovector electric and magnetic nucleon FFs at $m_\pi \sim 300$ MeV using TMF [41], DWF [42], hybrid [37] and Clover fermions [43]. Experimental data are shown with the filled green circles accompanied with Kelly’s parameterization shown with the dashed line. Right: Axial nucleon FFs. The solid line is a dipole fit to experimental data for $G_A(Q^2)$ combined with pion pole dominance to get the solid curve shown for $G_p(Q^2)$.

TMF and those obtained using the hybrid action on a larger volume, differ at small Q^2 where $G_p(Q^2)$ increases rapidly due to the pion-pole behavior. This may indicate that volume effects are not negligible on FFs such as $G_p(Q^2)$, which are strongly affected by the pion-pole.

3.2 Results on nucleon moments

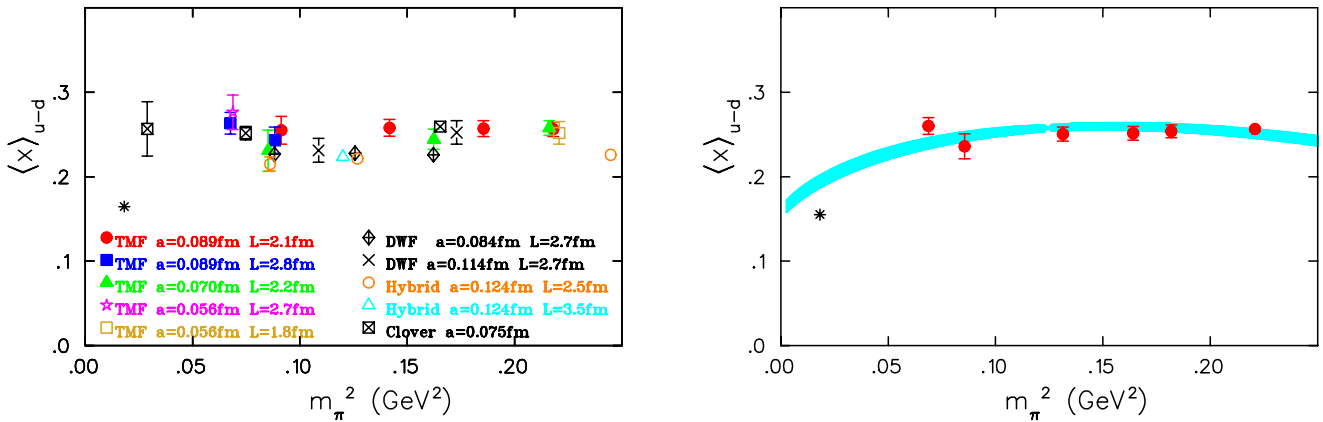


Figure 16: Left: Recent LQCD results on the isovector $A_{20}^{u-d} = \langle x \rangle_{u-d}$. The physical point is from Ref. [44]. Right: Chiral fit to the continuum extrapolated TMF results using HB χ PT.

In this section we show results on the nucleon matrix element of the one-derivative operators

$\bar{u}\gamma_{\{\mu}\overleftrightarrow{D}_{\nu\}}u - \bar{d}\gamma_{\{\mu}\overleftrightarrow{D}_{\nu\}}d$ and $\bar{u}\gamma_5\gamma_{\{\mu}\overleftrightarrow{D}_{\nu\}}u - \bar{d}\gamma_5\gamma_{\{\mu}\overleftrightarrow{D}_{\nu\}}d$ in the \overline{MS} scheme at a scale $\mu = 2$ GeV. In Fig. 16 we compare recent LQCD results on the isovector momentum fraction using TMF [45], Clover fermions from QCDSF [38], DWF from RBC-UKQCD [46] and LHPC [47] with different lattice spacings, and using a hybrid action by LHPC [37]. The moment of the helicity distribution $\tilde{A}_{20}^{u-d} = \langle x \rangle_{\Delta u - \Delta d}$ shows a similar behaviour. All collaborations, except LHPC, use non-perturbatively computed renormalization constants. The m_π -dependence of these moments in HB χ PT [48] are given by:

$$\langle x \rangle_{u-d} = C \left[1 - \frac{3g_A^2 + 1}{(4\pi f_\pi)^2} m_\pi^2 \ln \frac{m_\pi^2}{\lambda^2} \right] + \frac{c_8(\lambda^2)m_\pi^2}{(4\pi f_\pi)^2}, \quad \langle x \rangle_{\Delta u - \Delta d} = \tilde{C} \left[1 - \frac{2g_A^2 + 1}{(4\pi f_\pi)^2} m_\pi^2 \ln \frac{m_\pi^2}{\lambda^2} \right] + \frac{\tilde{c}_8(\lambda^2)m_\pi^2}{(4\pi f_\pi)^2}.$$

Using $\lambda^2 = 1$ GeV² and the TMF results we obtain the band shown in Fig. 16, which yields a value higher than experiment. This is also true for $\langle x \rangle_{\Delta u - \Delta d}$. The very recent result by QCDSF [38] at $m_\pi \sim 180$ MeV remains higher than experiment and highlights the need to understand such deviations.

3.3 Study of excited state contributions

As we have demonstrated in the previous sections, there are discrepancies between LQCD results and well measured quantities such as g_A . In this section we examine whether excited state contributions could be a possible origin of such discrepancies. This is done by performing a high-statistics analysis using $N_f = 2 + 1 + 1$ TMF configurations with $m_\pi \sim 380$ MeV at $a = 0.08$ fm. In order to probe effects of excited states the sink-source time separation was increased from about 1 fm used for the TMF results shown in the previous sections to about 1.5 fm for g_A and to 1.9 fm for $\langle x \rangle_{u-d}$ [49]. The insertion time of the operator from the source was fixed at 0.7 fm for g_A and at 0.85 fm for $\langle x \rangle_{u-d}$.

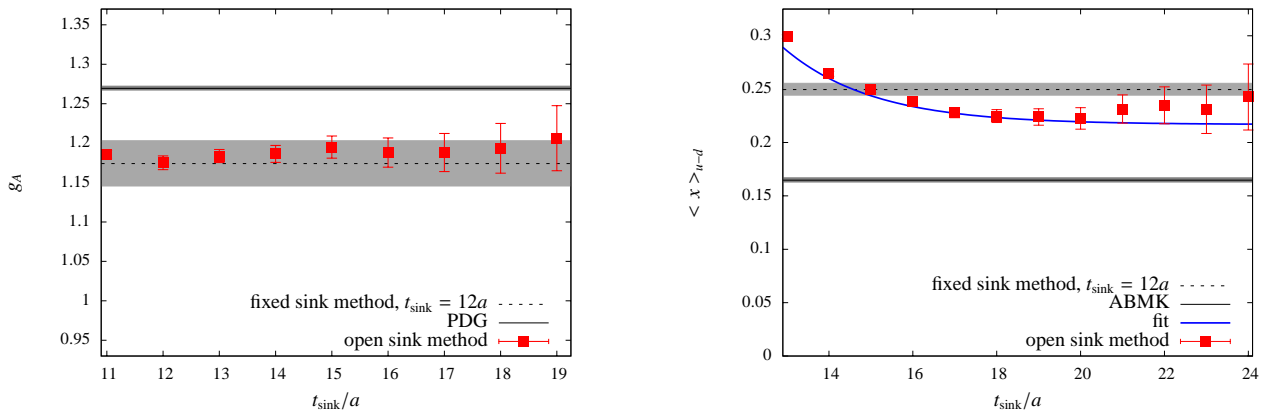


Figure 17: LQCD results on g_A (left) and $\langle x \rangle_{u-d}$ (right) as a function of the sink-source time separation. The larger grey band is the the value obtained by using a sink-source separation of about 1 fm.

From the results shown in Fig. 17 we conclude that, for $m_\pi = 380$ MeV, g_A shows no contamination from excited states, whereas $\langle x \rangle_{u-d}$ decreases by about 10% as compared to the value found for source-sink time separation of about 1 fm showing that excited state contributions are responsible for at least part of the discrepancy between LQCD and the experimental value.

3.4 Nucleon spin

Assuming that disconnected contributions remain small for pion masses down to about 300 MeV, we can evaluate the total spin carried by quarks in the nucleon considering only the connected contributions. In Fig. 18, we show results using $N_f = 2$ TMF for pion masses of 270 MeV $< m_\pi < 500$ MeV [45] and results obtained using a hybrid action of DWF on a staggered sea [37]. As can be seen, both sets of data are in qualitative agreement and at the physical pion mass they both lead to a total spin of $J^u \sim 1/4$ and $J^d \sim 0$ for the u- and d-quarks, respectively.

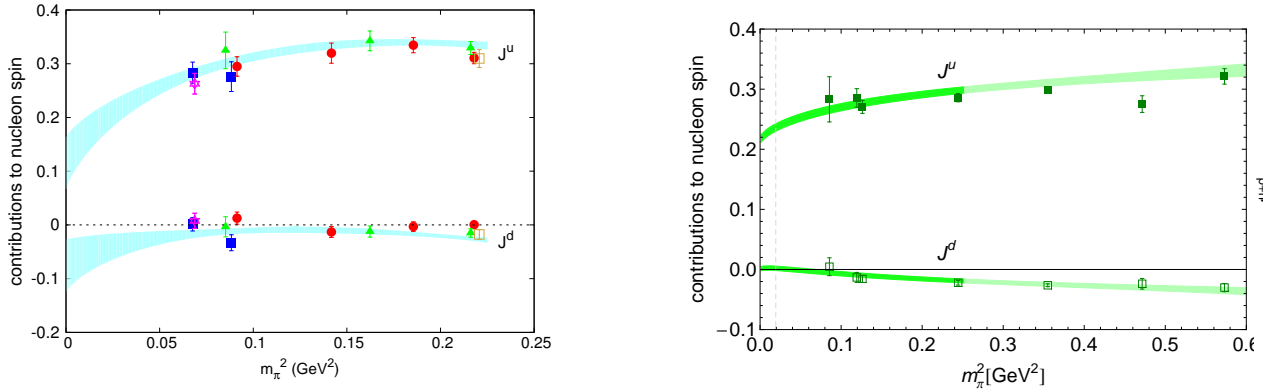


Figure 18: Total spin for u- and d- quarks, for TMF (left) [45] and for a hybrid action (right) [37].

4 N to Δ transition form factors

The nucleon is a spin-1/2 particle, and therefore its transverse charge densities do not exhibit a quadrupole pattern, nor do they encode any information on its shape. Such information can however be obtained from the $\gamma^*N \rightarrow \Delta$ transition charge densities. It is customary to characterize the N to Δ transition in terms of the three Jones–Scadron FFs, G_{M1}^* , G_{E2}^* and G_{C2}^* , denoting the magnetic dipole, electric quadrupole and Coulomb quadrupole transitions respectively [50]:

$$\langle \Delta(p', s') | j_\mu | N(p, s) \rangle = \mathcal{A} \bar{u}_{\Delta\sigma}(p', s') \left[G_{M1}^*(q^2) K_{\sigma\mu}^{M1} + G_{E2}^*(q^2) K_{\sigma\mu}^{E2} + G_{C2}^*(q^2) K_{\sigma\mu}^{C2} \right] u_N(p, s) \quad (11)$$

where $\mathcal{A} = i\sqrt{\frac{2}{3}} \left(\frac{m_\Delta m_N}{E_\Delta(\mathbf{p}') E_N(\mathbf{p})} \right)^{1/2}$. The magnetic dipole transition FF is the dominant one and has been accurately measured. Deformation is encoded in the ratios EMR and CMR, given by

$$\text{EMR} = -\frac{G_{E2}^*}{G_{M1}^*} \quad \text{CMR} = -\frac{Q_+ Q_-}{4M_\Delta^2} \frac{G_{C2}^*}{G_{M1}^*}, \quad (12)$$

with $Q_\pm \equiv \sqrt{(M_\Delta \pm M_N)^2 + Q^2}$. Dedicated experiments have yielded accurate measurements of the EMR and CMR excluding a zero value. This implies deformation in the N/Δ system as illustrated in Fig. 19.

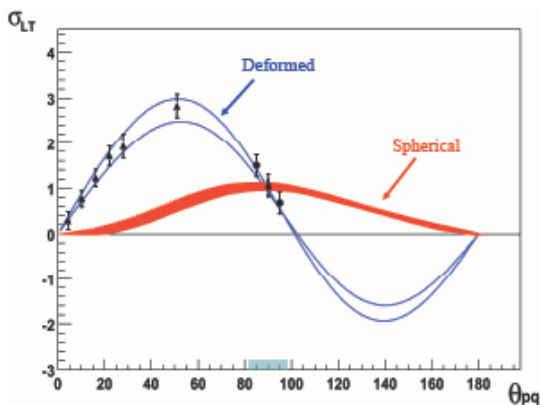


Figure 19: Precise data at $Q^2 = 0.126 \text{ GeV}^2$ strongly “suggesting” deformation in the N/Δ system [51, 52].

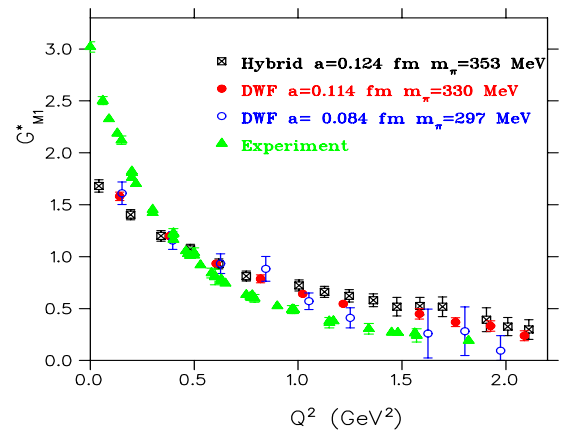


Figure 20: Experimental and LQCD results on the magnetic dipole FF G_{M1}^* versus Q^2 .

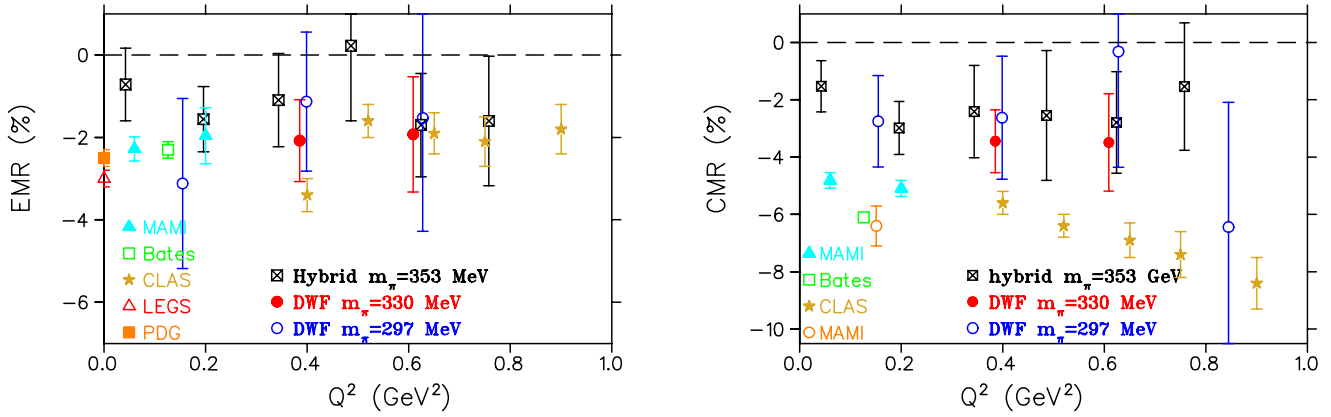


Figure 21: Results on EMR (left) and CMR (right).

The N to Δ transition FFs can be calculated within LQCD in a similar way to the FFs of the nucleon by evaluating the Δ - N three-point function associated with the EM current and the Δ and N two-point functions and forming the ratio

$$R_\sigma(\Gamma, \vec{q}, t) = \frac{G_\sigma(\Gamma, \vec{q}, t)}{G_{ii}^{\Delta\Delta}(\vec{0}, t_f)} \left[\frac{G_{ii}^{\Delta\Delta}(\vec{0}, t_f)}{G^{NN}(\vec{p}_i, t_f - t)} \frac{G_{ii}^{\Delta\Delta}(\vec{0}, t)}{G^{NN}(\vec{p}_i, t)} \right]^{1/2} \quad (13)$$

which yields, in the plateau region, the N to Δ matrix element of the EM current. A number of techniques have been implemented to accurately extract the sub-dominant quadrupole form factors such as optimized sources that isolate the two quadrupoles from the dominant magnetic dipole and coherent sinks that increase the statistical accuracy [42].

Recent LQCD results are shown in Figs. 20 and 21 using a hybrid action of $N_f = 2 + 1$ staggered fermion simulations and domain wall valence quarks, as well as $N_f = 2 + 1$ DWF simulated by the RBC-UKQCD collaborations with lowest pion mass of about 300 MeV [53]. The slope of G_{M1}^* at low Q^2 remains smaller than what is observed in experiment underestimating $G_{M1}^*(0)$ i.e. one observes the same effect as for the nucleon form factors. Since G_{E2}^* and G_{C2}^* are underestimated at low Q^2 like G_{M1}^* is, taking ratios may remove some of these discrepancies. Indeed the EMR shown in Fig. 21 is in better agreement with experiment than the magnetic dipole FF, whereas CMR approaches the experimental values as the pion mass decreases. Despite the increase in statistics, the errors on the sub-dominant ratios when using DWF are large and to produce results at lower than 300 MeV pion masses to a 20% accuracy one would need to increase significantly the number of statistically independent evaluations.

The Δ - N axial-vector matrix element $\langle \Delta(p', s') | A_\mu^3 | N(p, s) \rangle$ can be written as

$$\mathcal{A} \bar{u}_\Delta^\lambda(p', s') \left[\left(\frac{C_3^A(q^2)}{m_N} \gamma^\nu + \frac{C_4^A(q^2)}{m_N^2} p'^\nu \right) (g_{\lambda\mu} g_{\rho\nu} - g_{\lambda\rho} g_{\mu\nu}) q^\rho + C_5^A(q^2) g_{\lambda\mu} + \frac{C_6^A(q^2)}{m_N^2} q_\lambda q_\mu \right] u_N(p, s), \quad (14)$$

where the dominant FFs $C_5^A(q^2)$ and $C_6^A(q^2)$ are analogous to the nucleon $G_A(q^2)$ and $G_p(q^2)$, respectively. The Δ - N matrix element of the pseudo-scalar current is given by

$$2m_q \langle \Delta(p', s') | P^3 | N(p, s) \rangle = \mathcal{A} \frac{f_\pi m_\pi^2 G_{\pi N\Delta}(q^2)}{m_\pi^2 - q^2} \bar{u}_{\Delta\nu}(p', s') \frac{q_\nu}{2m_N} u_N(p, s). \quad (15)$$

Using the axial Ward identity one obtains the relation: $C_5^A(q^2) + \frac{q^2}{m_N^2} C_6^A(q^2) = \frac{1}{2m_N} \frac{G_{\pi N\Delta}(q^2) f_\pi m_\pi^2}{m_\pi^2 - q^2}$. Pion pole dominance relates C_6^A to $G_{\pi N\Delta}$ through $\frac{1}{m_N} C_6^A(q^2) \sim \frac{1}{2} \frac{G_{\pi N\Delta}(q^2) f_\pi}{m_\pi^2 - q^2}$, which leads to the non-diagonal Goldberger-Treiman (GT) relation

$$G_{\pi N\Delta} f_\pi = 2m_N C_5^A \quad (16)$$

In Fig. 22 we show results on the dominant axial FFs and on the ratio $G_{\pi N\Delta} f_\pi / 2m_N C_5^A$, which should be unity if the GT relation holds. This ratio approaches unity for $Q^2 > 0.5 \text{ GeV}^2$ [53].

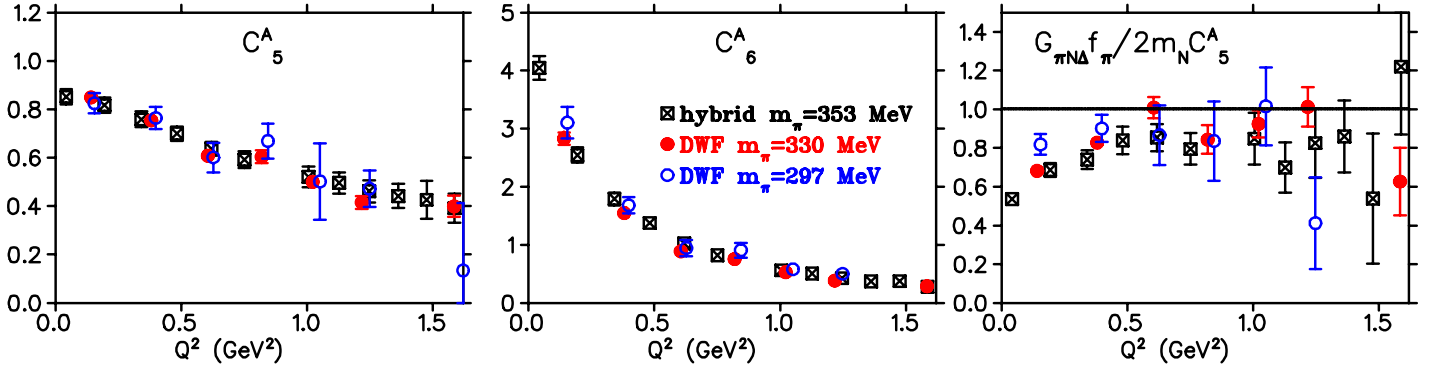


Figure 22: The dominant axial N to Δ FFs and the ratio of Eq. (16) using a hybrid action and DWF.

5 Δ form factors

The Δ matrix element of the EM current $\langle \Delta(p', s') | j^{\mu} | \Delta(p, s) \rangle$ can be written in terms of 4 FFs:

$$-\bar{u}_{\Delta\alpha}(p', s') \left\{ \left[F_1^*(q^2) g^{\alpha\beta} + F_3^*(q^2) \frac{q^{\alpha} q^{\beta}}{(2M_{\Delta})^2} \right] \gamma^{\mu} + \left[F_2^*(q^2) g^{\alpha\beta} + F_4^*(q^2) \frac{q^{\alpha} q^{\beta}}{(2M_{\Delta})^2} \right] \frac{i\sigma^{\mu\nu} q_{\nu}}{2M_{\Delta}} \right\} u_{\Delta\beta}(p, s) \quad (17)$$

with e.g. the quadrupole FF given by: $G_{E2} = (F_1^* - \tau F_2^*) - \frac{1}{2}(1 + \tau)(F_3^* - \tau F_4^*)$, where $\tau \equiv -q^2/(4M_{\Delta}^2)$.

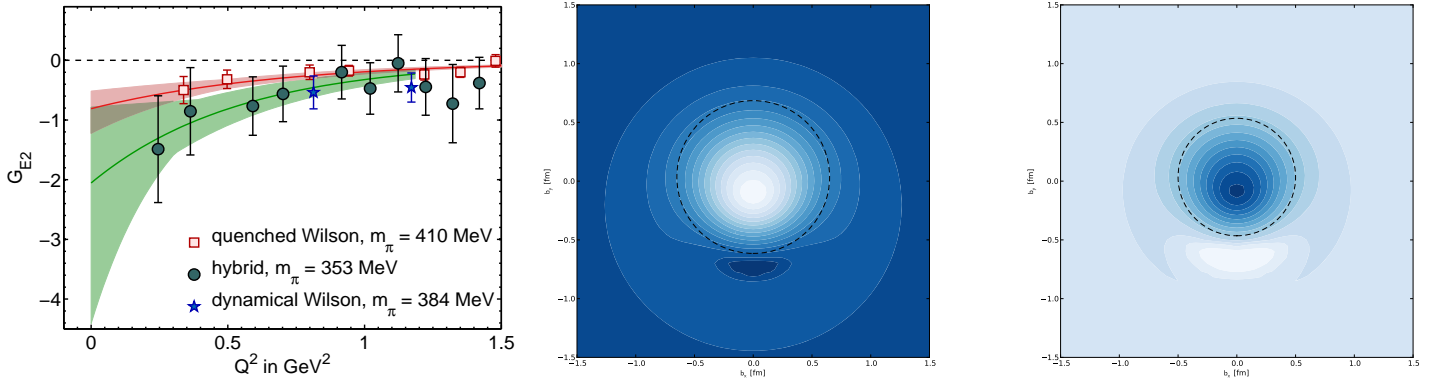


Figure 23: Left: LQCD results on the Δ electric quadrupole FF. Contours of Δ (middle) and Ω^- (right), with 3/2 spin projection along the x-axis. Dark colors denote small values.

Using LQCD results on G_{E2} one can obtain the transverse charge density of a Δ in the infinite momentum frame [54, 55]. This is shown in Fig. 23, where a Δ with spin 3/2 projection along the x-axis is elongated along the spin axis [54]. In the same figure we also show the corresponding charge density of the Ω^- [56], which shows a similar deformation as the Δ .

The Δ matrix elements of the axial-vector current $\langle \Delta(p', s') | A_{\mu}^3 | \Delta(p, s) \rangle$ is given by

$$-\frac{1}{2} \bar{u}_{\alpha}(p', s') \left[g^{\alpha\beta} \left(g_1(q^2) \gamma^{\mu} \gamma^5 + g_3(q^2) \frac{q^{\mu}}{2M_{\Delta}} \gamma^5 \right) + \frac{q^{\alpha} q^{\beta}}{4M_{\Delta}^2} \left(h_1(q^2) \gamma^{\mu} \gamma^5 + h_3(q^2) \frac{q^{\mu}}{2M_{\Delta}} \gamma^5 \right) \right] u_{\beta}(p, s) \quad (18)$$

LQCD results on the dominant FFs g_1 and g_3 are shown in Fig. 24. The Δ axial charge is derived from $g_1(0)$. The Δ matrix element of the pseudo-scalar current $\langle \Delta(p', s') | P^3 | \Delta(p, s) \rangle$ is given by

$$-\bar{u}_{\alpha}(p', s') \frac{f_{\pi} m_{\pi}^2}{2m_q(m_{\pi}^2 - q^2)} \left[g^{\alpha\beta} G_{\pi\Delta\Delta}(q^2) \gamma^5 + \frac{q^{\alpha} q^{\beta}}{4M_{\Delta}^2} H_{\pi\Delta\Delta}(q^2) \gamma^5 \right] u_{\beta}(p, s), \quad (19)$$

in terms of two $\pi\Delta\Delta$ pseudo-scalar FFs [57], of which $G_{\pi\Delta\Delta}$ is shown in Fig. 24.

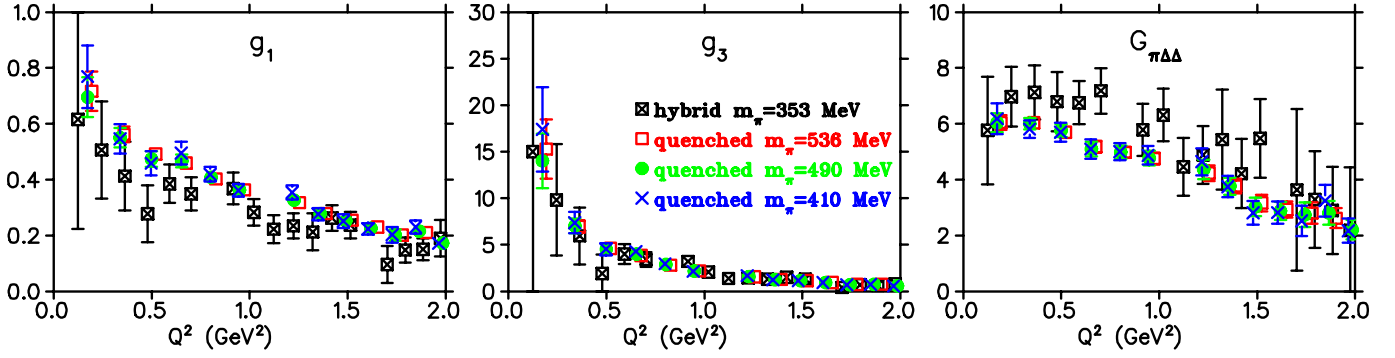


Figure 24: LQCD results on the dominant axial g_1 and g_3 , and pseudo-scalar $G_{\pi\Delta\Delta}$ Δ FFs in the quenched theory and using a hybrid action of DWF on a staggered sea [57].

6 Combined chiral fit

Having a set of lattice results for the axial nucleon charge [35], the axial $N - \Delta$ transition FF, $C_5^A(0)$ [53] and the Δ axial charge, allows us to perform a combined fit to all three quantities using HB χ PT in the SSE scheme [58, 59, 60].

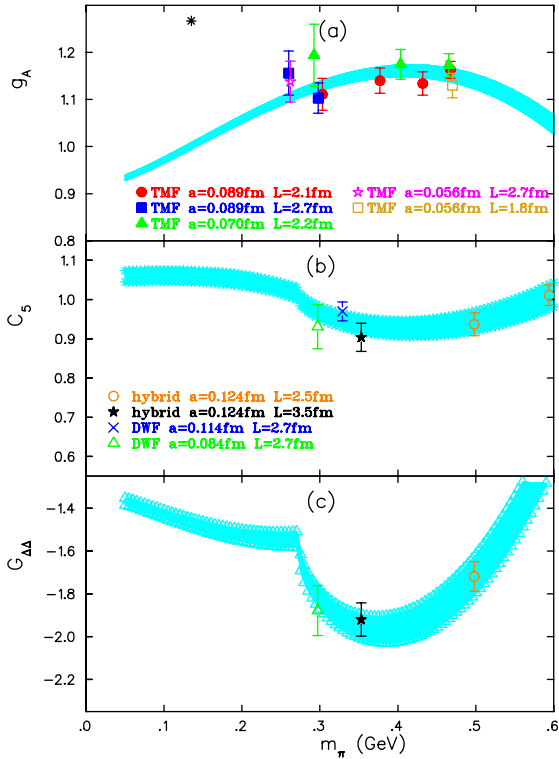


Figure 25: Combined chiral fits: (a) g_A with $N_f = 2$ TMF [35]; (b) Real part of axial N to Δ transition FF $C_5(0)$ [53]; (c) Real part of Δ axial charge $G_{\Delta\Delta} = -3g_1(0)$ [57].

7 Conclusions

We have shown that lattice QCD successfully reproduces the low-lying baryon spectrum using different discretization schemes. Understanding nucleon structure within LQCD is a fundamental issue that is being addressed by a number of lattice collaborations [12, 37, 42, 36, 61, 43]. Using similar techniques one can study transitions and resonant properties and in this work we have reviewed results on the

ρ -meson width, on the N to Δ transition FFs and the Δ FFs. The latter are difficult to measure experimentally and therefore LQCD provides valuable input on these quantities. The study of the complete N/Δ system enables one to extract the axial couplings from a combined chiral fit to LQCD results on the nucleon and Δ axial charges and the axial N to Δ form factor $C_5(0)$ [57]. Performing such a fit to lattice results in the pion mass range from 500 MeV to 300 MeV, does not reproduce the experimental value of g_A . Gauge configurations with pion masses below 200 MeV are becoming available enabling the evaluation of these key observables at near physical quark mass parameters. Using these simulations, combined with a detailed study of lattice systematics, are expected to shed light on the origin of the observed discrepancies.

Acknowledgments: I would like to thank all members of ETMC, as well as E. Gregory, J. W. Negele, T. Sato, A. Tsapalis and M. Vanderhaeghen for a very constructive and enjoyable collaboration. I am grateful to G. Koutsou and T. Korzec for their valuable comments on this manuscript. This research was partly supported by the Cyprus Research Promotion Foundation under contracts TECHNOLOGY/ΘΕΠΠΣ/0308(BE)/17, ΔΙΕΘΝΗΣ/ΣΤΟΧΟΣ/ 0308/07 and ΔΙΑΚΡΑΤΙΚΕΣ/ΚΥ-ΓΑ/0310/02 and by the Research Executive Agency of the European Union under Grant Agreement number PITN-GA-2009-238353 (ITN STRONGnet). DWF configurations were provided by the RBC and UKQCD collaborations and the forward propagators by the LHPC. Finally, I would like to thank A. Faessler and J. Wambach for inviting me to this enjoyable school.

References

- [1] G. Endrodi, Z. Fodor, S. D. Katz, K. K. Szabo, JHEP **1104**, 001 (2011).
- [2] Z. Fodor, S. D. Katz, [arXiv:0908.3341].
- [3] P. de Forcrand, PoS **LAT2009**, 010 (2009).
- [4] F. Karsch, Nucl. Phys. **A783**, 13-22 (2007).
- [5] P. Hagler, Phys. Rept. **490**, 49-175 (2010).
- [6] A. V. Belitsky, A. V. Radyushkin, Phys. Rept. **418**, 1-387 (2005). [hep-ph/0504030].
- [7] C. E. Hyde, K. de Jager, Ann. Rev. Nucl. Part. Sci. **54**, 217-267 (2004).
- [8] M. Diehl, Phys. Rept. **388**, 41-277 (2003).
- [9] X. Ji, J. Phys. G24, 1181 (1998).
- [10] D. Drechsel, B. Pasquini, M. Vanderhaeghen, Phys. Rept. **378**, 99-205 (2003).
- [11] B. C. Pearce, J. Speth, A. Szczurek, Phys. Rept. **242**, 193-232 (1994).
- [12] C. Alexandrou, PoS **LATTICE2010**, 001 (2010); C. Alexandrou, [arXiv:0906.4137].
- [13] S. Aoki (HAL Collaboration), Prog. Part. Nucl. Phys. **66**, 687-726 (2011).
- [14] M. J. Savage, [arXiv:1110.5943].
- [15] M. K. Joos et al. (Jefferson Lab Hall A Collaboration), Phys. Rev. Lett. **84**, 1398 (2000); O. Gayou et al., Phys. Rev. C **64**, 038202 (2001); V. Punjabi et al., Phys. Rev. C **71**, 0555202 (2005); C. E. Hyde-Wright, K. de Jager, Ann. Rev. Nucl. Part. Sci. **54**, 217 (2004).
- [16] C.F. Perdrisat, V. Punjabi, M. Vanderhaeghen, Prog. Part. Nucl. Phys. **59**, 694, (2007); J. Arrington, C. D. Roberts and J. M. Zanotti, J. Phys. G **34**, S23 (2007).
- [17] K. de Jager, Prog. Part. Nucl. Phys. **61**, 311 (2008); K. Jager, AIP Conf. Proc. **1056**, 412 (2008); K. de Jager, Int .J. Mod. Phys. E19, 844 (2010).
- [18] C. Morningstar, PoS **LATTICE2008**, 009 (2008); C. Morningstar, *et al.* [arXiv:1109.0308].
- [19] J. M. Bulava, *et al.*, Phys. Rev. **D79**, 034505 (2009).
- [20] S. Durr *et al.*, JHEP **1108**, 148 (2011); S. Aoki *et al.* [PACS-CS], Phys. Rev. **D81**, 074503 (2010).
- [21] K. Jansen, C. Urbach, Comput. Phys. Commun. **180**, 2717-2738 (2009).
- [22] M. Hasenbusch, Phys. Lett. **B519**, 177-182 (2001).
- [23] S. Durr, *et al.* [BMW] Science **322**, 1224-1227 (2008).

- [24] C. Alexandrou *et al.* [ETMC], Phys. Rev. **D80**, 114503 (2009); Phys. Rev. **D78**, 014509 (2008).
- [25] T. Kaneko *et al.* [JLQCD], PoS **LAT2007**, 148 (2007); A. Jüttner *et al.* [RBC-UKQCD], PoS C **D09** (2009) 010; D. Brömmel *et al.* [QCDSF-UKQCD] Eur. Phys. J. C **51**, 335 (2007); D. Brömmel *et al.* [QCDSF], Eur. Phys. J. C **51**, 335 (2007); F. D. R. Bonnet *et al.*, Phys. Rev. D. **72**, 054506 (2005).
- [26] B. B. Brandt, A. Juttner, H. Wittig, [arXiv:1109.0196].
- [27] R. Frezzotti, V. Lubicz and S. Simula, Phys. Rev. D **79**, 074506 (2009).
- [28] R. Sommer, Nucl. Phys. **B411**, 839-854 (1994).
- [29] J. Frison *et al.*, arXiv:1011.3413; S. Aoki *et al.* (PACS-CS), arXiv:1011.1063; S. Aoki *et al.*, Phys. Rev. D **76**, 094506 (2007); M. Göckeler *et al.* (QCDSF), PoS **LATTICE2008**, 136 (2008).
- [30] X. Feng, K. Jansen, D. B. Renner, Phys. Rev. **D83**, 094505 (2011); PoS **LAT2009**, 109 (2009).
- [31] G. S. Bali, S. Collins, A. Schafer, Comput. Phys. Commun. **181**, 1570-1583 (2010);
- [32] R. Babich *et al.* [arXiv:1012.0562]; G. S. Bali, S. Collins, C. Ehmman, [arXiv:1110.2381].
- [33] C. Alexandrou, K. Hadjiyiannakou, G. Koutsou, A. O’Cais, A. Strelchenko, [arXiv:1108.2473].
- [34] C. Alexandrou, M. Constantinou, T. Korzec, H. Panagopoulos, F. Stylianou, Phys. Rev. **D83**, 014503 (2011); PoS **Lattice 2010**, 224 (2010).
- [35] C. Alexandrou *et al.* [ETMC], Phys. Rev. **D83**, 045010 (2011).
- [36] T. Yamazaki *et al.*, Phys. Rev. **D79**, 114505 (2009).
- [37] J. D. Bratt *et al.* [LHPC], Phys. Rev. **D82**, 094502 (2010).
- [38] D. Pleiter *et al.* [QCDSF/UKQCD], PoS **LATTICE2010**, 153 (2010).
- [39] A. Ali Khan *et al.* [QCDSF], Phys. Rev. D **74**, 094508 (2006).
- [40] T. R. Hemmert, M. Procura and W. Weise, Phys. Rev. D **68**, 075009 (2003).
- [41] C. Alexandrou *et al.*, Phys. Rev. **D83**, 094502 (2011).
- [42] S. N. Syritsyn, *et al.*, Phys. Rev. **D81**, 034507 (2010).
- [43] S. Capitani, B. Knippschild, M. Della Morte, H. Wittig, PoS **LATTICE2010**, 147 (2010); B. B. Brandt *et al.*, Eur. Phys. J. ST **198**, 79-94 (2011).
- [44] S. Alekhin, J. Blumlein, S. Klein, S. Moch, Phys. Rev. **D81**, 014032 (2010).
- [45] C. Alexandrou *et al.* [ETMC], Phys. Rev. **D83**, 114513 (2011).
- [46] Y. Aoki *et al.*, Phys. Rev. **D82**, 014501 (2010).
- [47] S. N. Syritsyn *et al.*, [arXiv:1111.0718].
- [48] D. Arndt, M. Savage, Nucl. Phys. **A697**, 429 (2002); W. Detmold, W. Melnitchouk, A. Thomas, Phys. Rev. D **66**, 054501 (2002).
- [49] S. Dinter *et al.*, Phys. Lett. **B704**, 89 (2011).
- [50] V. Pascalutsa, M. Vanderhaeghen, S. N. Yang, Phys. Rept. **437**, 125-232 (2007).
- [51] C. N. Papanicolas, Eur. Phys. J. **A18**, 141-145 (2003).
- [52] N. F. Sparveris *et al.* [OOPS Collaboration], Phys. Rev. Lett. **94**, 022003 (2005).
- [53] C. Alexandrou, G. Koutsou, J. W. Negele, Y. Proestos, A. Tsapalis, Phys. Rev. **D83**, 014501 (2011).
- [54] C. Alexandrou, T. Korzec, G. Koutsou, C. Lorce, J. W. Negele, V. Pascalutsa, A. Tsapalis, M. Vanderhaeghen, Nucl. Phys. **A825**, 115-144 (2009).
- [55] C. Alexandrou, T. Korzec, G. Koutsou, T. Leontiou, C. Lorce, J. W. Negele, V. Pascalutsa, A. Tsapalis, Phys. Rev. **D79**, 014507 (2009).
- [56] C. Alexandrou, T. Korzec, G. Koutsou, J. W. Negele, Y. Proestos, Phys. Rev. **D82**, 034504 (2010).
- [57] C. Alexandrou, E. B. Gregory, T. Korzec, G. Koutsou, J. W. Negele, T. Sato, A. Tsapalis, Phys. Rev. Lett. **107**, 141601 (2011); PoS **LATTICE2010**, 141 (2010).
- [58] T. R. Hemmert, M. Procura, W. Weise, Phys. Rev. **D68**, 075009 (2003).
- [59] M. Procura, Phys. Rev. **D78**, 094021 (2008).
- [60] F. -J. Jiang, B. C. Tiburzi, Phys. Rev. **D78**, 017504 (2008).
- [61] S. Collins *et al.*, Phys. Rev. **D84**, 074507 (2011).